A. Airoldi, P. Bettini, P. Panichelli, M.F. Oktem, G. Sala
Chiral Topologies for Composite Morphing Structures - Part I: Development of a Chiral Rib for Deformable Airfoils
Physica Status Solidi. B, Basic Solid State Physics, Vol. 252, N. 7, 2015, p. 1435-1445
doi:10.1002/pssb.201451689

CHIRAL TOPOLOGIES FOR COMPOSITE MORPHING STRUCTURES - PART I: DEVELOPMENT OF A CHIRAL RIB FOR DEFORMABLE AIRFOILS

Alessandro Airoldi*, Paolo Bettini*, Paolo Panichelli*, Mehmet F. Oktem, Giuseppe Sala***
***Dept. of Aerospace Science and Technology, Politecnico di Milano**
Via La Masa, 34 – 20156 Milano – Italy
****Dept. of Mechanical Engineering, Yildirim Beyazit University**
Çankırı Caddesi Çiçek Sokak No:3, Ulus, Altındağ, Ankara - Turkey

Abstract

The paper moves from a technological process developed in previous works to produce chiral honeycombs made of thin composite laminates. Such approach is applied in this work to manufacture the morphing ribs for a variable camber wing-box. The specifications for such components are obtained by developing a finite element model of a demonstrator, which is designed taking into account aeroelastic performances, structural and technological issues. In the first part of the paper, the design of such a demonstrator is presented and the role of composite chiral ribs with auxetic behaviour is outlined. Production, testing and numerical studies of manufacturing trials are performed to assess the technological process applied to small-sized chiral units made of different materials, to investigate their mechanical properties and to validate a numerical approach for design and analysis. A complete chiral composite rib is then produced and tests are carried out to verify the overall structural response and to validate the numerical approach.

1 Introduction

In the aerospace field, the term morphing structures is usually referred to aerodynamic surfaces that can progressively change their shape, so to enhance versatility and efficiency in the

generation of the aerodynamic forces required for motion, guidance and control of the vehicles. Morphing structural concepts are studied to replace the moveable rigid surfaces that are currently used to vary and adapt the aerodynamic shapes, such as aileron, flaps, rudders and spoilers, as well as to provide new functionalities for optimizing the shape of the aircraft for different missions and mission segments. The key aspect to achieve such objectives is the development of structures with low or tuneable compliance properties in morphing directions, so to achieve a controlled shape variation under the action of actuation, aerodynamic and inertia forces. At the same time, morphing components should collect and transmit the resultant of aerodynamic forces to other structural parts without failure or undesired deformation. Although the exploitation of structural compliance to change the shape of aerodynamic surfaces dates back to the early years of flight history, as in the examples reported by Anderson [1] or in the variable camber wing proposed by Parker [2], the aforementioned requirements are particularly challenging for modern aircraft, due to high flight speeds and consequently high aerodynamic loads. For this reason, morphing structures have received a renewed interest only in the last years, due the availability of new materials and actuation concepts. A large number of solutions that implement different morphing concepts, such as in-plane or out-of-plane wing transformation or variation of profile cambering, by exploiting the properties of innovative and smart materials, is listed in Barbarino et al. [3] and in Sofla et al. [4]. Although some of the proposed structural architectures are basically internal mechanisms made of rigid parts covered by flexible skins, such as the one presented by Monner [5], several solutions adopt a compliant and deformable internal structures, such as in [6-11].

Structural configurations presenting auxetic behaviour may offer interesting advantages for the development of a deformable internal structure of a morphing aerodynamic surface, since negative Poisson's ratios involve high shear moduli and an inherent resistance to local shape variations. In particular, auxetic honeycombs based on chiral topologies [12,13] have been

proposed by several authors to design the internal structure of deformable, variable-camber airfoils. Chiral tessellations consist of circular nodes connected by ligaments and present an inherent design flexibility thanks to the possible choice of different topologies and the variation of geometrical parameters, such as node diameters, ligaments lengths and thickness (see Alderson et al. [14]).

The examples provided in literature [7-10, 15-16] show that airfoils with an internal chiral structure deform under the action of external forces assuming new shapes characterized by smooth curvatures without angular points. A distinctive feature of chiral cores studied in literature is the possibility of changing the camber of the profile maintaining a thickness distribution along the chord that is close to the original one. This is fundamental for the aerodynamic efficiency of the surface and is closely related to the auxetic response of the internal structure. Such performances can also be achieved by spikes that connect the upper and lower surfaces by means of elastic hinges, such as in the solution proposed by Campanile and Sachau [6]. However the control of the airfoil thickness is more efficiently obtained by a chiral honeycomb, since it can withstand compression without the risk of buckling and does not need any elastic hinge to accomplish shape variations, thus eliminating structural weak points. Alternative solutions based on internal compliant mechanism are proposed by Previtali and Ermanni [11], where the control of shape variation is obtained by optimizing the geometry and the material properties of a network of internal ligaments. Such solutions obtain the required performances for a pre-defined shape variation and are optimized for a given actuation lay-out, whereas the adoption of a structural concept such as the chiral honeycomb offers the possibility of multiple combinations of actuation forces, so to potentially provide a variety of morphing functionalities with a single structural design. Such aspect is related to the aforementioned resistance of chiral topologies to local shape variations. This involves the contributions of a relatively large part of the honeycomb to accomplish the deformation imposed by concentrat-

ed or distributed forces, which is eventually obtained with an overall change of shape at a moderate local strain level. The studies reported in Spadoni and Ruzzene [9] and Airoldi et al. [10] prove the versatility of chiral honeycomb to obtain different types of global and local shape variation still maintaining an efficient aerodynamic shape and meeting realistic requirements regarding aeroelastic and structural constraint. Moreover, the availability of a structural concept that is inherently adapted to obtain smooth shape variations for different types of actuation concepts, including passive solutions without actuation, can suggest new and unforeseen types of morphing solutions, which can efficiently exploit the work done by aerodynamic forces, as it is exemplified by Airoldi et al. [16]. Such aspects motivated the researches to develop morphing solutions based on airfoils hosting chiral cores, exploiting their design flexibility, versatility and to develop manufacturing techniques to produce such types of structural topologies. Although, other configurations can be adopted to develop auxetic cellular cores [17], which can potentially have similar performance of chiral tessellations, solutions based on chiral topologies have been extensively studied and proved to be well-suited for morphing applications.

Moreover, adoption of composite materials increases the potential performances and the design flexibility of chiral honeycombs, as it was shown by Bettini et al. [15], and allows the application of different manufacturing strategies.

A technology for the production of thin-walled chiral composite honeycomb made of laminated plies was devised in [15] and applied to produce composite chiral units that were experimentally characterized under the action of forces acting in different planes, for morphing and crashworthiness applications [15, 18]. Such promising technological results inspired the conceptual design of a morphing wing-box in Airoldi et al. [10], with the capability of increasing its camber and amplifying the lift when the angle of attack increases, thus providing a significant increment of the slope in the curve of the lift vs. angle of attack. Since the behaviour of

this aerodynamic surface resembled the one of a marine sail, the concept was defined “chiral sail”.

Moving from these results, this paper presents the development of a chiral rib for a demonstrator implementing the chiral sail concept. The design of the demonstrator is developed in the first part of the paper and the requirements for the chiral ribs are outlined. Technological trials are carried out to produce small-sized chiral units by adopting glass fiber and carbon fiber reinforced composite layers. Such units are tested to investigate their response and numerically analysed to validate the approaches followed for the design of the ribs. A chiral composite rib is finally produced and tested in various load conditions. Test results are compared with numerical predictions to assess the validity of the overall development process.

2 General design of a chiral sail demonstrator

The chiral sail concept that was developed by Airoldi et al. [10] is based on a symmetric airfoil with rigid leading and trailing edge connected by a central morphing part. The two rigid edges can rotate around hinges, set at a distance x_{g1} and x_{g2} from the leading edge, as it shown in Fig. 1-a. The central morphing part occupies a length $x_2 - x_1$ of the airfoil chord and hosts a composite hexa-chiral core, which is characterized by the length of ligaments, L, and the radius of the circular node, r. The deformation of the central part under the action of the aerodynamic pressure can induce the rotation of the rigid edges and the composite chiral core is designed to obtain a final shape characterized by a smooth curvature of the airfoil mid-line, without an excessive variation of the thickness distribution along the chord. The core is connected to an external flexible skin, which collects the aerodynamic forces.

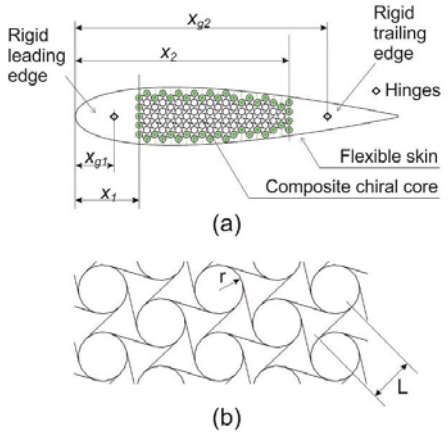

Fig. 1 – Scheme of the chiral sail airfoil (a) and details of the hexa-chiral topology (b)

Design was accomplished by using an aeroelastic model in an optimization process aimed at maximizing the slope of the lift vs. angle of attack curve. The lift is proportional to the lift coefficient, C_L, which for a rigid airfoil turns out to be linearly dependent on the angle of attack, α, between the airfoil chord and the direction of the asymptotic wind, V_∞. In the morphing concept proposed, when the angle of attack is increased, the airfoil changes its camber, as it shown in Fig. 2-a, and the derivative of the lift coefficient, $C_{L/\alpha}$, is amplified. Such effect can be effectively exploited for all the surfaces that are designed to stabilize the motion of the vehicle, since the stabilizing effect is proportional to $C_{L/\alpha}$ and to the area of the aerodynamic surface, so that smaller surfaces could be adopted. An asymptotic velocity of 42 m/s was selected for the design, considering a possible future experiment in one of the wind tunnel facilities available at the Aerospace Science and Technology Dept. of Politecnico di Milano. The chord of the airfoil was set equal to 1 m.

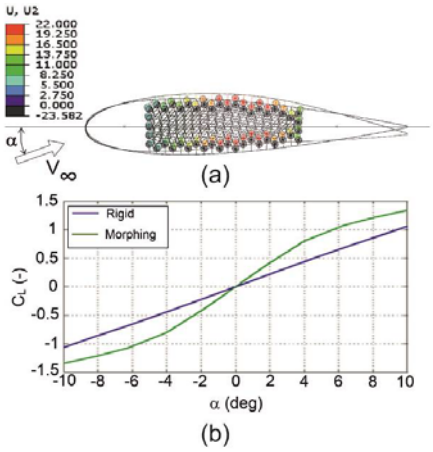

Fig. 2 – Deformation of the optimized configuration of the chiral sail (a) and lift coefficient vs. angle of attack curve for the morphing and rigid airfoil (b)

The graph reported in Fig. 2-b is referred to the optimized configuration defined in [10] and indicates that the chiral sail achieves a double $C_{L/\alpha}$ with respect to the rigid case, with a maximum displacement in the central chiral part of δ_{max} = 22 mm, as it is reported in the displacement contour presented in Fig. 2-a. The geometrical parameters of the optimized configuration are x_{g1} = 0.12 m x_{g2} =0.78 m , x_1 = 0.20 m and x_2 = 0.90 m. The parameters of the hexa-chiral topologies, shown in Fig. 1-b, were set to L = 19.3 mm and r = 10.3 mm.

The aeroelastic model used in [10] was a bi-dimensional model, so that it represented a wing where the chiral honeycomb core occupies the whole span. The optimization process leads to very thin ligaments, with a thickness of 0.232 mm. The design took also in consideration the characteristic of the flexible skin, which was modelled as a generic orthotropic plate by directly defining the coefficient of the stiffness matrix shown in Eq. 1:

$$\begin{Bmatrix} \mathbf{N} \\ \mathbf{M} \end{Bmatrix} = \begin{bmatrix} \overline{\mathbf{A}} & \overline{\mathbf{B}} \\ \overline{\mathbf{B}}^T & \overline{\mathbf{D}} \end{bmatrix} \begin{Bmatrix} \boldsymbol{\varepsilon}_0 \\ \boldsymbol{\kappa} \end{Bmatrix} \qquad \text{Eq. 1}$$

where **N** and **M** are vectors containing the three components of the forces per unit width and of the moments per unit width applied to the plate, whereas $\boldsymbol{\varepsilon_0}$ is the vector of the three components of mid-plane strains and, finally, $\boldsymbol{\kappa}$ is the vector including the two bending curvatures and the warping of the plate. $\overline{\mathbf{A}}$ and $\overline{\mathbf{D}}$ in Eq. 1 are 3 x 3 submatrices that represent the membrane stiffness andthe bending stiffness of the plate, respectively. The 3 x 3 submatrix $\overline{\mathbf{B}}$ represents the coupling terms between membrane and bending behavior.

The optimization process confirmed the basic requirements of low axial stiffness and adequate bending stiffness that were defined by Gandhi and Anusonti-Inthra [19] for a morphing skin. An axial stiffness in the range of 20 N/mm ÷ 30 N/mm was selected in the chord direction, whereas a bending stiffness of about 620 Nmm was found necessary to avoid bubbling of the skin under the action of the pressure and possible consequent detrimental effects on aerodynamic performances.

According to the calculations, in the optimal configuration, the stiffness of the chiral core is adequate to sustain the external skin, to maintain an efficient aerodynamic shape during morphing and to transmit the forces to the rigid leading and trailing edges. However, the production of a three-dimensional wing demonstrator with a thin-walled composite chiral core occupying the whole wingspan has been considered technologically complicate. Therefore, the design of the demonstrator was carried out considering a configuration based on chiral ribs that have to perform the same role of the diffused honeycomb core. Such configuration is presented in Fig. 3-a, with three ribs distributed along a total span, *b*. Nominally, the central rib has to collect the aerodynamic pressure along a span $b_{rib} = b/2$, which defines the pitch of the ribs, though, in the demonstrator, the lateral ribs will be loaded by half of such force. A new requirement for the skin is introduced, since the pressure tends to deflect the skin panel in each bay, between the ribs. Therefore, skin must provide an adequate bending stiffness in the span direction. Among the skin concepts that were proposed for morphing structures by

Thill et al. [20], a feasible solution to satisfy all skin requirements is offered by composite corrugated laminates, which are characterised by strongly anisotropic properties and have been proposed by several authors for morphing applications [21, 22]. In following section, it will be shown that the material and geometrical parameters of a skin with a classical corrugated shapes, such as the one presented in Fig. 3-b, can be selected to meet the prescribed requirements by using analytical formulations for the evaluation of the stiffness properties of an equivalent homogenized orthotropic plates [23].

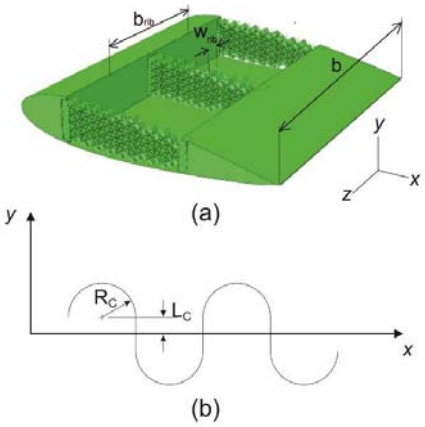

Fig. 3 – Configuration of demonstrator with chiral ribs (a) and parameters of corrugated laminates proposed for the morphing skin (b)

Assuming that the skin provides an adequate response and neglecting its stiffness contribution in the morphing direction, a stiffness per unit width, $K'_{airfoil}$, can be defined for the internal structure of the wing considering the ratio of the total lift acting on the wing, L_w, and the maximum vertical displacement due to morphing, δ_{max}, divided by the span, b. Such expression is given in Eq. 2.

$$K'_{airfoil} = \frac{dK_{airfoil}}{dz} = \frac{1}{b}\frac{L_{wing}}{\delta_{\max}} = \frac{l_{wing}}{\delta_{\max}} \qquad \text{Eq. 2}$$

where $K_{airfoil}$ is the stiffness of the entire structure and l_{wing} is the lift per unit wing span.

The load acting on a discrete rib, L_{rib}, is collected along the a span b_{rib}. Such load can be calculated knowing lift per unit wing span : $L_{rib} = l_{wing} b_{rib}$

Since the rib is a chiral honeycomb, the stiffness per unit width required to the rib to obtain the same deflection of the structure with a diffused chiral core is:

$$K'_{rib} = K'_{airfoil} \frac{b_{rib}}{w_{rib}} \qquad \text{Eq. 3}$$

Accordingly, the ratio of the rib stiffness per unit width to the one of the diffused chiral core is equal to the ratio b_{rib}/w_{rib}. In the demonstrator design, a ratio of 10 was selected. Since the in-plane stiffness of the chiral honeycomb is determined by the bending stiffness of ligaments, which varies with the cube of ligament thickness, the increment of thickness required for the solution with chiral ribs can be estimated to $\sqrt[3]{b_{rib}/w_{rib}} = 2.15$, in order to obtain the same stiffness of the solution with the diffused core. Considering the optimal solution obtained for the diffused chiral core, the indicative thickness of the ligaments should be set at about 0.5 mm.

3 Finite element model of the demonstrator and specification of ribs and skin

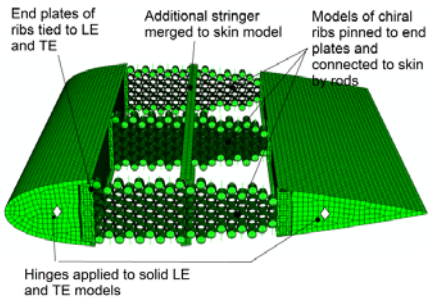

Fig. 4 – Finite element model of the demonstrator

A finite element model of the demonstrator was developed and solved by using Simulia/Abaqus Standard code. The model, without the skin, is shown in Fig. 4. It consists of solid leading and trailing edges, meshed by first-order solid 8-noded brick elements (*C3D8* element [24]), which were characterized by using an isotropic material with a low elastic modulus, and coated by first-order 4-noded shell elements (*S4* element [24]), which were modelled by using the elastic properties of a 2 mm thick aluminium alloy sheet. The lateral sides of such elements were defined as rigid bodies and were pinned to the ground reference frame at the same location of the hinges defined in the optimal solution in Airoldi et al. [10]. The chiral ribs were meshed by using first-order 4-noded shell elements (S4 element [24]) with a typical size of 2.5 mm. The composite material considered for the composite chiral rib is the SEAL CC90/ET443 plain weave carbon fabric pre-preg, with properties that were characterized in Bettini in al. [15] and are reported in Table 1. In the technological process presented in [15], the nodes are obtained by superposition and bonding of ligaments, so that they turns out to have two times the thickness of the ligaments. Although such rule was followed in the models developed for the optimization process, it can be observed that a large part of the chiral honeycomb weight turns out to be concentrated at the nodes, which do not undergo severe bending conditions as the ligaments do. Accordingly, it was decided to model nodes having the same thickness of the ligaments to reduce the weight cost and to introduce the required modifications in the technological process, as it will be presented in the following sections. However, the ligament thickness was increased with respect to the values previously estimated and was set to 0.6 mm.

Eliminato:

Table 1 – Properties of carbon-reinforced composite plies used in the design of the demonstrator

E_{11}	MPa	56550
E_{22}	MPa	56550

v_{21}	-	0.05
G_{12}	MPa	4040
ply thickness	mm	0.1

All the elements belonging to the nodes at the boundaries of the ribs were linked to the centres of the chiral nodes by using a system of rigid beams. The connections between the chiral core and the skin were modelled by using rods, which were represented by metallic beams with a 1 mm x 5 mm rectangular section (elements B31 [24]) hinged both to the centre of the chiral nodes close to the skin and to the skin nodes, according to the same technique presented in [10].

At the forward and rear boundaries, the centres of the chiral nodes were hinged to pins set between two vertical plates, which can be seen in Fig. 4. Pins were modelled by beam elements (elements B31 [24]) with a circular section of the same diameter of chiral nodes and material properties of an aluminium alloy. Such type of constraint allows a free rotation of the chiral nodes connected to the leading and trailing edges and leads to reduce the stress levels on the surrounding ligaments, as it was observed in [10]. The external surfaces of the plates were tied to the solid models of leading and trailing edges by using a technique to join dissimilar meshes available in the solver code [24].

The skin was characterized with first-order, 4-noded shell elements (*S4R* [24]) with a typical size of 20 mm. The elements were characterized by introducing the values of the orthotropic stiffness matrix defined in Eq. 1. The mesh of a central reinforcement is also visible in Fig. 4. Such component shares the nodes with the ones of the skin and was characterized with the values of its stiffness matrix.

The value of the axial and bending stiffness of the skin along the chord were set to the target levels identified in the optimization process, whereas the bending stiffness in the span direc-

tion was progressively increased until a level of $1.5 \cdot 10^5$ Nmm and $1.5 \cdot 10^6$ Nmm for the skin and the central reinforcement, respectively. By adopting such values, the deflection of the skin in the design load condition was limited to a negligible fraction of the overall vertical displacement. The surface of the model was loaded with the aerodynamic pressure field obtained in the aeroelastic solution of the optimized configuration in [10]. The contour of the obtained vertical displacements, reported in Fig. 5, shows that the morphing performance is qualitatively similar to one of the bi-dimensional model and is characterized by a lower maximum displacement, δ_{max}, equal to about 20 mm.

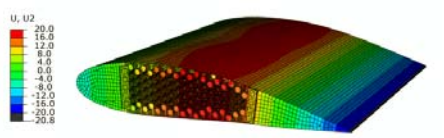

Fig. 5 – Contour of vertical displacement in the design condition

The contour also shows that the skin experiences a small additional deflection between the ribs. To evaluate the stiffness levels that can be obtained in a constructive solution, the stiffness properties of a corrugated laminate with the configuration shown in Fig. 3-b were evaluated by applying the expressions reported in Eq. 4, which are taken from [23]. The A_{11}, A_{22}, D_{11} and D_{22} symbols in Eq. 4 refer to the properties of the plane laminate used in the corrugation, which are obtained by applying Classical Lamination Theory once that the laminate lay-up has been defined. The values with the overbars are the properties of a plate equivalent to the corrugated laminate, with axis 1 corresponding to x direction in Fig. 3-a and axis 2 corresponding to z direction in the same figure.

$$\overline{A}_{11} = \frac{4R_c}{\left(\frac{\pi R_c}{A_{11}} + \frac{l_2}{D_{11}}\right)}$$

$$\overline{D}_{11} = \frac{2R_c}{\pi R_c + 2L_c} D_{11} \qquad \text{Eq. 4}$$

$$\overline{D}_{22} = \frac{1}{4R_c}\left(l_2 A_{22} + \pi R_c D_{22}\right)$$

$$\text{with} \quad l_2 = \frac{4L_c^3}{3} + 2\pi L_c^2 R_c + 8 L_c R_c^2 + \pi R_c^3$$

The geometrical parameter R_c and L_c in Eq. 4 are the ones defined in Fig. 3-b. If a corrugated laminate with R_c = 6.0 mm, L_c = 1.0 mm and a $[0]_6$ lay-up of the CC90/ET443 SEAL plies is used, with the properties reported in Table 1, an axial stiffness and a bending stiffness in the chord direction of 20.5 N/mm and 587.3 Nmm are obtained. Such values acceptably fulfil the requirements for the skin set in [10]. The bending stiffness in the span direction turns out to be equal to $1.7 \cdot 10^6$, which is one order of magnitude higher than the stiffness adopted in the numerical assessment of the demonstrator design. Such increment of stiffness has no effects on the morphing performances, since the skin must be as stiffer as possible in the span direction to properly collect the aerodynamic forces within the bay and to transmit them without undergoing excessive deformation. Moreover, the high stiffness values in the span direction, which are a consequence of the strong anisotropy of the corrugated plate, provide a significant contribution to the bending stiffness of the entire aerodynamic surface in non-morphing directions.

4 Technological trials and experimental activities for the development of a composite chiral rib

The activities performed for the design of the chiral sail demonstrator confirm the feasibility of the concept and specify the characteristic of the composite chiral ribs required to achieve the desired morphing performances. The technology to manufacture the chiral rib of the demonstrator was based on the process developed in Bettini et al. [15] for thin-walled, laminated

composite chiral units. Such technological process consists in two separate steps, namely the production of curved ligaments and the bonding of pre-cured ligaments to obtain a chiral topology where nodes are created by the superposition of ligaments ends. Originally, the procedure was assessed considering 7-noded chiral units with a ligament length L=75 mm and a node radius r = 18 mm. Such dimensions are larger than the ones required for the chiral ribs that were designed for the chiral sail demonstrator. Hence, the technology was assessed to produce smaller chiral units with the new geometrical parameters, L=19.3 mm and r = 10.3 mm. Moreover, modification were introduced to avoid excessively thick nodes, according to the considerations introduced in the previous section of the paper.

The metallic mould used to produce the ligaments is shown in Fig. 6-a. Figure 6-b refers to the shape of a ligament and gives a generic example of lamination sequence, with more plies in the central parts of the ligaments and a smaller number of plies in the curved ends, thus reducing the thickness of the nodes obtained by ligaments superposition. Ligament shape also features small hooks at the curved ends to facilitate the final assembly. An autoclave vacuum-bag process was adopted to produce a 280 mm wide curved laminate, shown in Fig. 6-a, which was subsequently cut to obtain the 20 mm wide ligaments that are aligned on the mould in Fig. 6-c.

The second phase of the technological process is performed to superimpose and bond the ligaments in a second autoclave process. An epoxy adhesive film, 3M AFK-163-2K, is set on the ligaments curved end, as it is shown for a couple of ligaments in Fig. 6-c. Positioning is carried out by using cylinders endowed with slots, where the hooks of the ligaments are inserted, thus obtaining the chiral unit shown in Fig. 6-d. An assembly mould, shown in Fig. 6-e, is adopted in the final autoclave vacuum bag process. A key feature of the manufacturing methodology is represented by the introduction in such assembly of silicon rubber inserts, made of RECKLI^{TM} SI compound with a shore hardness 20. As it was discussed in [15] such ele-

ments, under the action of the autoclave pressure and of their own thermal expansion, exert a significant pressure on the adherends during the process and improve the quality of bonding.

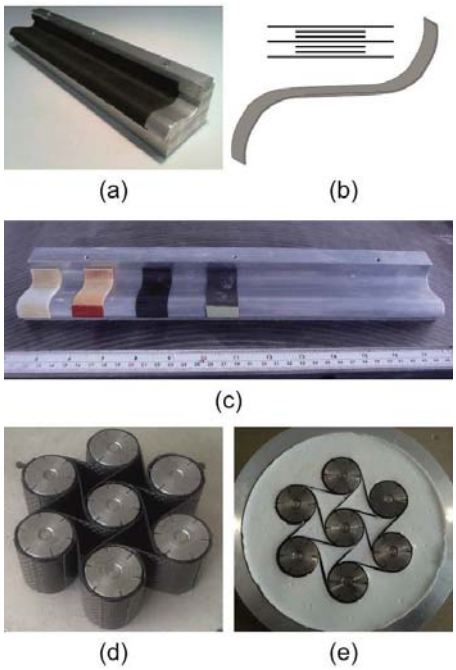

Fig. 6 – Technological process: ligament shape (a), ligament lay-up (b), manufactured ligaments (c), assembled unit (d) and assembly mould with silicon rubber inserts (e)

The carbon-reinforced fabric considered for the demonstrator design, with properties reported in Table 1, was used for the production of two chiral units, a stiff one with a lay-up $[0]_8$ and a thickness of 0.7 mm and a compliant one with a lay-up $[0]_3$ and a thickness of 0.3 mm. Another set of ligaments was produced by using an E-glass-reinforced pre-preg, SEAL EE48 REM, with a plain weave textile style and the properties reported in Table 2. Such ligaments were used to produce a stiff glass-reinforced chiral unit, with a lay-up $[0]_{17}$ and a thickness of 0.95 mm and a compliant unit, with an angle-ply lay-up $[+45/-45]_{5s}$ and a thickness of 0.50 mm. Some of the units produced are shown in Fig. 7-a.

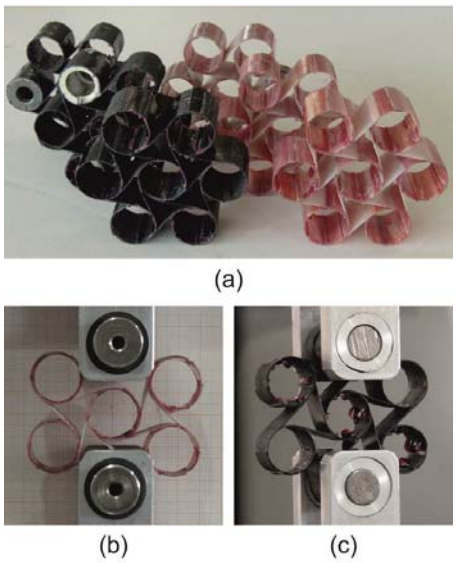

Fig. 7 – Chiral units produced (a) and test lay-out for a glass reinforced unit (b) and a carbon reinforced unit (c)

Table 2 – Properties of glass-reinforced composite plies used during technological development

E_{11}	MPa	24000
E_{22}	MPa	2400
ν_{21}	-	0.11
G_{12}	MPa	4043
ply thickness	mm	0.055

Carbon and glass reinforced chiral units were subjected to tensile tests, by inserting steel pins into two nodes. Pins were connected to light alloy clevises, which are shown in Fig. 7-b and 7-c, which are referred to experiments on a glass and on a carbon unit, respectively. The pins

were fixed to the heads of an MTS 858 servo-hydraulic system, with a full scale range set to 1.5 kN. For some of the stiff units, pins were not directly set in contact with the internal surface of the cylindrical nodes to avoid promoting a premature damage. Load application nodes were filled with epoxy resin that was subsequently drilled to house the pins, as it is shown in one unit in Fig. 7-b. All tests were conducted in displacement control mode, at a loading rate of 1 mm/min.

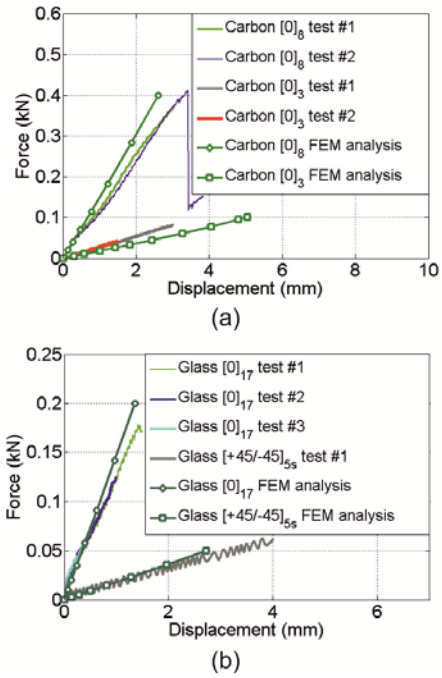

Fig. 8 – Experimental tests and numerical correlation for carbon (a) and glass (b) chiral units

The results of the experimental tests are reported in Fig. 8. Such results confirm that the stiffness of thin-walled composite chiral units with given geometrical parameters can be largely varied by changing the lamination sequence of the ligaments. Responses also indicate that the

experimental force vs. displacement curve is substantially linear, though some non-linear behaviour can be observed in the initial phase of tests performed on some of the stiff units, which can be attributed to the yielding of the resin introduced in the end cylinders..

The stiff units made of carbon and glass reinforced ligaments have been tested until tensile failure. The failures obtained are presented in Fig. 9-a and Fig. 9-b for a carbon and a glass composite unit, respectively. Failure in the carbon unit occurred at 0.4 kN and was characterized by the debonding of one ligament connected to one of the superimposed cylinders. In the chiral unit produced in E-glass reinforced composite, failure occurred at 0.2 kN at the same location. Debonding can be observed in Fig. 9-b, though the breakage of one of the ligaments is also apparent. Indeed, ligaments tend to unwind around the cylindrical nodes when a tensile force is applied to a chiral network and such loading promotes the development of a mode I crack in the adhesive layers.

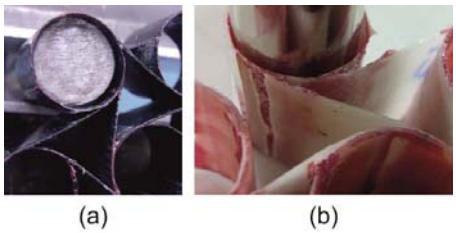

Fig. 9 – Experimental failure in carbon-reinforced (a) and glass-reinforced (b) chiral units

5 Validation and application of a numerical approach for rib design

Finite element models of the tests performed on the manufacturing trials were also developed, with ligaments represented by second order 8-noded shell elements (elements *S8R* [24]), having a typical size of about 1.5 mm.

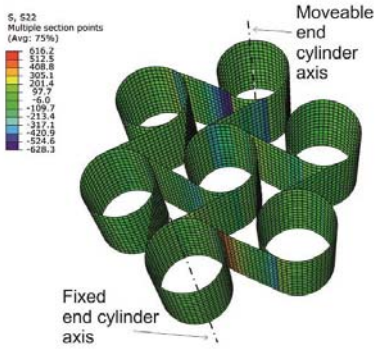

Fig. 10 – Numerical contour of longitudinal stress on carbon stiff unit model at failure loads

Lamination sequences were modelled taking into account the superposition of tapered ligaments. The load application pins were modelled by beams (elements *B31* [24]), which were connected to two reference nodes and left free to rotate. The beams where characterized with the properties of the steel pins used in the experiments. All the nodes of the two end cylinders of the units were linked by means of a kinematic coupling to such beams, which forces the nodes to follow the beam rotation as it were rigidly connected but leaves the possibility of radial motion. The model of the chiral unit is shown in Fig. 10, where the axes of the pins introduced in the upper and lower cylinder are represented. The end nodes of the lower pin were linked to a fixed reference node, whereas the ends of the upper pin were connected to a moveable reference node. Analyses were carried out by considering non-linear geometrical effects. The force vs. displacement numerical responses are included in Fig. 8. Considering the imprecisions in the lamination of tapered ligaments and the presence of the adhesive layers between the superposed ligaments, the numerical-experimental correlation is acceptable.

The finite element models of the chiral units can be used to investigate the failure conditions. The contour of longitudinal stress on the surface of the ligaments for the carbon unit cell is shown in Fig. 10, at a load of 0.4 kN, corresponding to the experimental failure load. It can

be observed that the ligaments close to the end cylinders undergo severe bending conditions, with longitudinal stress higher than 600 MPa. Such stress corresponds, according to the value given in Table 1, to a strain higher than 1%, which can be considered close to the failure strain for the carbon fabric material loaded in the reinforcement direction, which was evaluated in Bettini et al. [15]. The findings regarding the failure mode completely confirm the results obtained for the larger carbon units tested in [15], where failure was determined by debonding in a condition where maximum bending strength of ligaments was almost reached. Such findings indicate that a good bonding quality can be indeed obtained in the manufacturing process. For the carbon units with L = 19.3 mm and r = 10.3 mm tested in this work, the finite element model also provided an estimation of the unwinding bending moment per unit width that was applied to the ligament in correspondence of the experimental failure. Unwinding moment at failure turned out to be more than 50 Nmm/mm and such limit was used to verify the design of the chiral rib in composite material.

However, the model of the chiral rib was developed by using a less refined mesh than the one adopted for the analyses of the experiments on the chiral units and a linear analysis procedure was chosen. A convergence study was performed considering the glass fibre reinforced units with $[0]_{17}$ and $[+45,-45]_{5s}$ lay-ups. Models were developed by using first-order shell elements (*S4* elements [24]) at decreasing element size and linear analyses were performed by applying 0.2 kN to the stiff unit with $[0]_{17}$ lay-up and 0.05 kN to the compliant unit with $[+45,-45]_{5s}$ lay-up. For the smallest element size, non-linear analyses were also performed. The displacement obtained and the contour of longitudinal stress for two models of the compliant unit are shown in Fig. 11. Such figure also includes the results obtained at the same load levels by the analyses used to generate the force vs. displacement curves in Fig. 8, which were obtained by using second-order elements. For the compliant unit, the difference of displacements between the coarsest linear model and the most refined non-linear model with higher order elements is

of 3.7%. Most of the difference is due to activation of the non-linear analysis procedure. The maximum difference for the case of the stiff unit is 2%. The results also confirm the experiments carried out in [15], where a non-linear behaviour was detected for large displacements of chiral units.

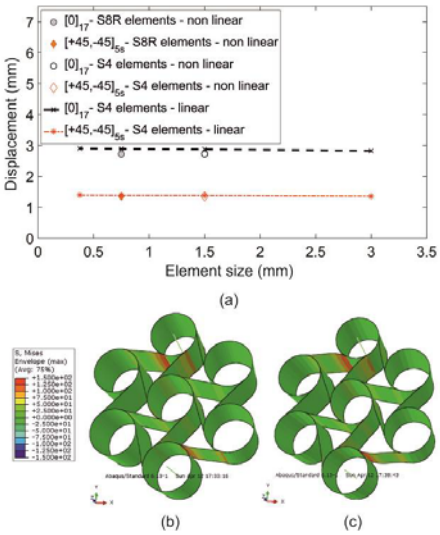

Fig. 11 – Convergence studies for the models of the glass chiral units (a) and stress contour in a refined non-linear model (b) and in a coarse linear model (c)

The contour of longitudinal stress reported in Fig. 11 are referred to the non-linear analyses of the compliant unit with first-order elements of 0.75 mm (Fig. 11-b) and to the linear analysis with first-order elements of 3 mm (Fig. 11-c). The maximum stress levels are acceptably captured by the coarse linear model, which was developed by using element type, size and analysis procedure identical to the ones selected for the ribs in the model of the entire demonstrator.

The contour of the longitudinal stress and of the bending moment per unit width in the central rib of the chiral sail demonstrator model is shown in Fig. 12, in correspondence of the design

conditions represented in Fig. 5. The most loaded ligaments are at the boundaries of the rib, which undergo stress conditions that are significantly higher than those obtained in the internal core. However, the maximum absolute value of the longitudinal stress components in the chiral honeycomb is below 250 MPa, as shown in Fig. 10-a. The bending moments are below 15 Nmm. Hence, according to previous experimental and numerical evaluations, the composite chiral rib can be considered verified with respect to failure risks in the test conditions.

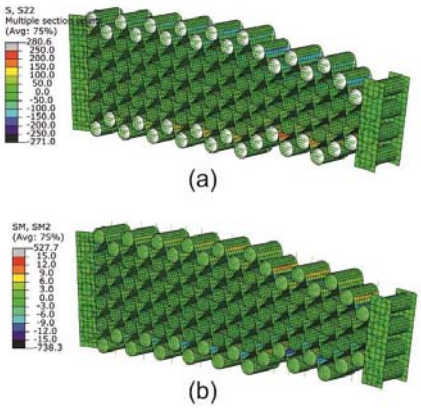

Fig. 12 – Numerical contour of longitudinal stress (a) and bending moment per unit width (b) in the central rib of the demonstrator model

6 Manufacturing and testing of the composite chiral rib

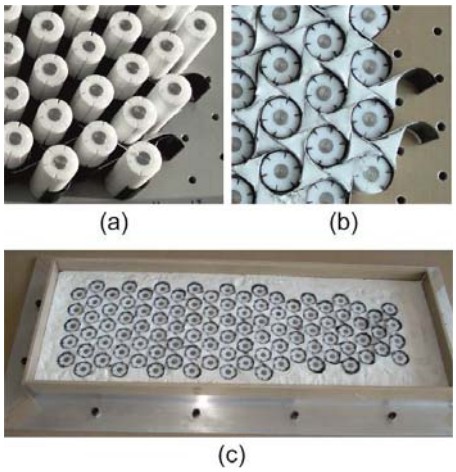

Fig. 13 – Rib production: positioning of ligaments (a), assembly (b) and final assembly mould (c)

One of the lateral ribs designed for the chiral sail demonstrator was manufactured to assess the technological process in the production of a structural composite component based on a chiral topology and to test the properties of such element. After a series of manufacturing trials, it was decided to apply a uniform lamination sequence with 5 carbon fabric plies for the ligaments. Additional metallic moulds, like the one in Fig. 6-a, were machined to reduce the number of autoclave cycles required for ligaments production. A light alloy plate was used to form the basis of the assembly mould, endowed with positioning holes in correspondence of the nodes of the chiral network. The preliminary positioning of the ligaments is shown in Fig. 13-a. A modification with respect to the original technology was introduced by using positioning cylinders made of polytetrafluoroethylene (PTFE), to facilitate the extraction of such elements at the end of the process. Silicon rubber inserts were separately produced and the final assembly was carried out progressively, first introducing a single PTFE cylinder, then ligaments hooked to such element and finally the rubber inserts. A phase of this process is

shown in Fig. 13-b. The complete mould, endowed with light alloy dams, is presented in Fig. 13-c.

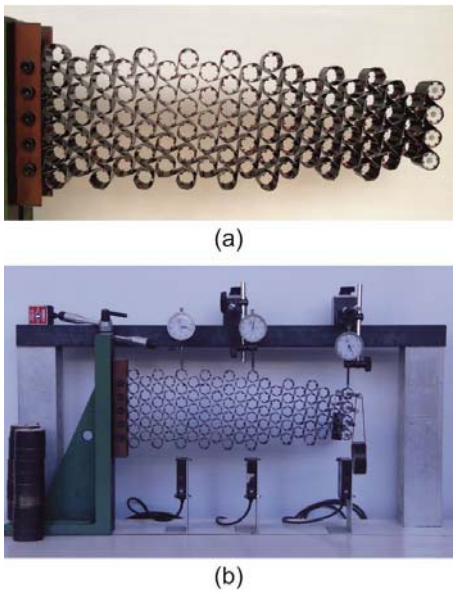

Fig. 14 – Rib produced (a) and experimental set-up (b)

The manufactured rib is presented in Fig. 14-a. It was easily extracted by the assembly mould and analysed without detecting any visible defects in the chiral composite network. A test to investigate the mechanical properties of the elements was conceived considering a configuration with all the nodes of the forward end pinned to a steel fixture and weights applied to other nodes at different stations. The PTFE positioning cylinders were re-inserted in all the nodes where constrains and loads were applied. Application of loads and constraints was accomplished by means of steel pins introduced in the central hole of the PTFE elements. The experimental set-up, shown in Fig. 14-b, includes a series of 0.5 kg weights, which were combined in different loading steps at three loading stations on the lower boundary of the rib. A set of laser transducers was adopted to measure the deflection of the lower node, in corre-

spondence of the loading stations, whereas the deflection of the upper nodes was measured by using micrometers, shown in Fig. 14-b.

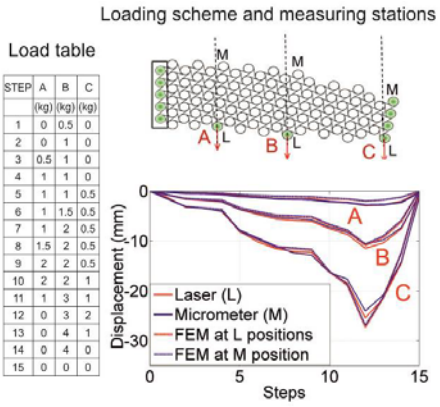

Fig. 15 – Experimental tests and correlation with numerical rib model

The experiments were performed though a series of loading steps characterized by different combinations of loads, which are reported in the table included in Fig. 15. In the first 13 steps, weights were progressively added at the different loading stations, indicated by the letters A,B and C in Fig. 15. Thereafter, in the last two steps, the rib was unloaded. A maximum deflection of 25 mm was obtained without observing any residual deformation at unloading. The finite element scheme of the rib was extracted from the model of the demonstrator shown in Fig. 4 and was separately analysed by applying boundary conditions corresponding to the ones of the test. The nodes at the clamped ends were constrained at a fixed reference frame by using the same methodology that was adopted to join the chiral ribs to the rigid leading and trailing edges of the demonstrator model. The loads were applied to the centres of the chiral nodes corresponding to stations A,B and C, shown in Fig. 15. The systems of rigid elements, which were used for the connection between the chiral core and the skin in the demonstrator model, was exploited to apply such loads. Correlation between the results of finite element analyses and the experiments showed that the manufactured rib is actually stiffer than the nu-

merical model. Such discrepancy can be attributed to the difficulties in modelling the real constraint conditions of the ligaments to the nodes. The superposition of ligaments and the excess of adhesive at the cusps between the ligaments and the nodes are likely to oppose the free bending of the ligament in the regions close to nodes. Such effect was not observed in the stiff carbon unit produced in the manufacturing trials, though it should be observed that the resin used to fill the end nodes, where the pin were inserted, may have added some compliance to the physical unit. Conversely, the compliant unit, which was tested without any filler in the nodes, turned out to be stiffer than the non-linear numerical model, as it is shown in Fig. 8. For the model of the chiral rib, an acceptable numerical-experimental correlation was obtained by increasing of 15% the nominal thickness of the ligaments, as it is presented in Fig. 15.

However, since a 15% increase of the ligament thickness approximately corresponds to an additional ply in the ligaments, the ligaments thickness adjusted for optimal correlation is very close to the thickness used in the demonstrator model. Hence, although the experiment carried out on the rib does not exactly represent the rib configuration and the loadings considered in the design condition of the demonstrator, the technological, numerical and experimental activities performed confirm the feasibility of the technological process and partially validate the numerical predictions obtained in the numerical model of the whole demonstrator.

7 Concluding remarks

The application of composite chiral networks for the development of morphing structures was successfully assessed in the activities presented in this paper. Moving from the conceptual design of a morphing wing and from preliminary technological achievements, a demonstrator of the chiral sail concept based on the development of chiral ribs was designed. The design process defined the characteristics of the chiral components and pointed out the ability of such

type of structures in controlling the shape variations during morphing. Moreover, strength requirements for the chiral components in design conditions were identified. The technological process, which had been originally developed for chiral units with relatively large geometrical dimensions, was applied to different types of materials and proved adequate to manufacture topologies with smaller ligament length and node radii. The activities performed on the units allowed the assessment of the numerical approach for the design of composite honeycomb core. Finally, the technology developed was successfully applied to produce the complete chiral rib, a complex component made of hundreds of ligaments, fulfilling the stiffness and strength requirements for the chiral sail demonstrator. The experiments performed on the rib confirm that a morphing component made of materials suitable for real-world aircraft structure can be manufactured according to a chiral auxetic topology. Moreover, the experimental activities validated the numerical approaches used in the design of the rib and confirmed that debonding of ligaments in tensile loading condition represents the most critical aspect of the proposed structural concept. Such aspect and the complexity of manufacturing process represent the most significant obstacles for the application of chiral composite honeycomb in aerospace structures with the capability of progressive shape variations. However, the promising results obtained in this work indicate that composite chiral networks have the potential to fulfil requirements regarding the functional performances of morphing structures. Moreover, the experience gained in the design and manufacturing of the composite rib can provide the guidelines for the development of new technological routes to simplify the process and improve the mechanical process of chiral composite honeycombs.

References

[1] J.D. Anderson, *A History of Aerodynamics and its Impact on Flying Machines*, Cambridge Unive. Press, New York/London/Cambrindge, England, U.K., 1999.

[2] H.F. Parker, *The Parker Variable Camber Wing*, NACA Rept. 77, 1920.

[3] S. Barbarino, O. Bilgen,, R.M. Ajaj, M.I. Friswell,. and D.J. Inman, A review of morphing aircraft, *Journal of Intelligent Material Systems and Structures*, **22**, 823-827, 2011.

[4] A.Y.N. Sofla, S, M.A. Meguid, K.T. Tan, W.K. Yeo, Shape morphing of aircraft wing: Status and challenges, *Materials and Design,* **31**, 1284-1292, 2010.

[5] H.P. Monner, Realization of an Optimized Wing Camber by Using Form-Variable Flap Structures, *Aerospace Science and Technology*, 5(7), 445–455, 2001.

[6] L.F. Campanile, and D. Sachau, The belt-rib concept: a structronic approach to variable camber, *Journal of Intelligent Material Systems and Structures*, **11**(3), 215-224, 2000.

[7] D. Bornengo, F. Scarpa, C. Remillat, Evaluation of hexagonal chiral structure for moprhing airfoil concept, *Journal of Aerospace Engineering*, **219**, 185-192, 2005.

[8] J. Martin, J.J. Heyder-Bruckner, C. Remillat, F. Scarpa, K. Potter and M. Ruzzene. The hexachiral prismatic wingbox concept, *Physica Status Solidi B,* **245**(3), 570-577, 2008.

[9] A. Spadoni and M. Ruzzene, Numerical and experimental analysis of chiral truss-core airfoils, *Journal of Mechanics of Materials and Structures,* **2**(5), 965-981, 2007.

[10] A. Airoldi, M. Crespi, G. Quaranta, G. Sala. Design of a morphing airfoil with composite chiral structure, *Journal of Aircraft,* **49**(4), 1008-1019, 2012.

[11] F. Previtali and P. Ermanni, Performances of a non-tapered 3D morphing wing with integrated compliant rib, *Smart Materials and Structures* **21**(5), 0550008, 2012.

[12] R.S. Lakes, Deformation mechanism in negative Poisson's ratio materials : structural aspects, *Journal of Materials Science and Technology,* **26**, 2287-2292, 1991.

[13] D. Prall and R.S. Lakes, Properties of a chiral honeycomb with a Poisson's ratio -1, *International Journal of Mechanical Science*, **39**, 305-314, 1996.

[14] A. Alderson, K. Alderson, D.D. Attard, K. Evans, R, Gatt, J. Grima et al, Elastic constants of 3-,4- and 6-connected chiral and anti-chiral honeycombs subject to uniaxail in-plane loading, *Composite Science and Technology,* **70**(7), 1042-1048, 2010.

[15] P. Bettini, A. Airoldi, G. Sala, L. Di Landro, M. Ruzzene and A . Spadoni, Composite Chiral Structures for Morphing Airfoils: Numerical Analyses and Development of a Manufacturing Process, *Composites Part B - Engineering*, **41**(2), 133-147,2010.

[16] A. Airoldi, G. Quaranta, A. Beltramin and G. Sala, Design of a morphing actuated aileron with chiral composite internal structures, *Advances in Aircraft and Spacecraft Science*, **1** (3), 329-349,2014.

[17] J. Ju, J.D. Summers, Compliant hexagonal periodic lattice structures having both high shear strength and high shear strain, *Materials and Design* **32**, 512-524, 2011.

[18] A. Airoldi, P. Bettini, M. Zazzarini, F. Scarpa*, Failure and Energy Absorption of Plastic and Composite Chiral Honeycombs*, in: Structures Under Shock and Impact XII, G. Schleyer and C.A. Brebbia (Eds.), WIT Press, Southampton, 2012.

[19] F. Gandhi, P. Anusonti-Inthra, Skin design for variable camber morphing aircraft, *Smart Materials and Structures,* **17**, 1-8, 2008.

[20] C Thill, J. Etches, I. Bond, K. Potter, P. Weaver, Morphing Skins, *The Aeronautical Journal*, **112**(1129), 117–139, 2008.

[21] T. Yokozeki, S. Takeda, T. Ogasawara and T. Ishikawa, Properties of corrugated composites for candidate flexible wing structures, *Composites Part A: Applied Science Manufacturing*, **37**(4), 1578-1586, 2006.

[22] C. Thill, J.A. Etches. I. Bond, K. Potter, P.M. Weaver and M.R. Wisnom, Investigation of trapezoidal corrugated arammid/epoxy laminates under large tensile displacements train-

verse to corrugation direction, *Composites Part A : Applied Science Manufacturing*, **41**,168-176, 2010.

[23] Y. Xia, M.I. Firswell, E.I. Saavedra Flores, Equivalent models of corrugated panels, *International Journal of Solids and Structures* ***49***, 1453-1462, 2012.

[24] Abaqus, *Analysis and User's Manual Version 6.13*, 2013.